Chapter VII: Studies on microstructure, cation distribution and magnetic properties of $Zn_xCo_{1-x}Cr_2O_4$ ($0.15 \leq x \leq 0.8$) nanoparticles.

7.1. Introduction

The cations and their distribution among A and B sites play a vital role in tuning the magnetic ordering temperature in $CoCr_2O_4$. It is interesting to investigate the effect of substitution by a third cation in $CoCr_2O_4$, which affect the magnetic exchange interactions and hence affecting the spin state of the system [Yamasaki et al. (2006); Tomiyasu et al. (2004)]. In this regard, Kochur et al. (2015) have studied cation distribution and valence state of transition metal ions in $Co_{1-x}Fe_xCr_2O_4$ (x=0.1, 0.2, 0.5). While certain Fe^{2+} ions were found in tetrahedral coordination, the Fe^{3+} ions found in both tetrahedral and octahedral sites. They have argued that a partly inverse spinel structure in which some of Fe ions substitute Co ion while other Fe ions substitute Cr ions. Later, Kumar at al. (2017) have studied the cation distribution dependent magnetic properties in $CoCr_{2-x}Fe_xO_4$(x=0.1-0.5). They have showed that Fe ions prefers towards the A site at x=0.1 and favor B site at x=0.5. Further, the quantitative analysis of Mossbauer spectra showed, while 60 % of Fe ions occupy tetrahedral site in x=0.1, they only observed 40% in x=0.5. However, Fe ions are equally distributed among A and B sites in x=0.3. Magnetic measurements show while, T_C increases from 102 K to 200 K, T_S increases from 26 K to 40 K with increase in Fe concentration from 0.1 to 0.5. The exciting results thus insist to discuss the mixing tetrahedral or octahedral sites by magnetic or non-magnetic ions after reducing the size of the particle to nanometer range. The cation distribution and magnetic properties reported in few chromites, have not been studied in Zn substituted $CoCr_2O_4$ nanoparticles so far. Hence, we examine the structural

and magnetic properties of $Zn_xCo_{1-x}Cr_2O_4$ (x=0.15, 0.2, 0.5, 0.8) nanoparticles. In this chapter, we have discussed the structural analysis and cation distribution in section 7.2.1 and magnetic properties in section 7.2.2. The conclusions are summarized in section 7.3.

7.2. Results

7.2.1. Structural and Microstructural analysis

7.2.1.1. X-ray Diffraction

Fig. 7.2.1 depicts the X-ray diffraction patterns of $Zn_xCo_{1-x}Cr_2O_4$ (x=0.15, 0.2, 0.5 and 0.8). The Bragg peaks observed at 30.45, 35.75, 43.5, 54, 57.5 and 63.1 degrees correspond to the planes (220), (311), (400), (422), (511) and (440) of the cubic phase of $CoCr_2O_4$ (JCPCS file no: 780711) respectively.

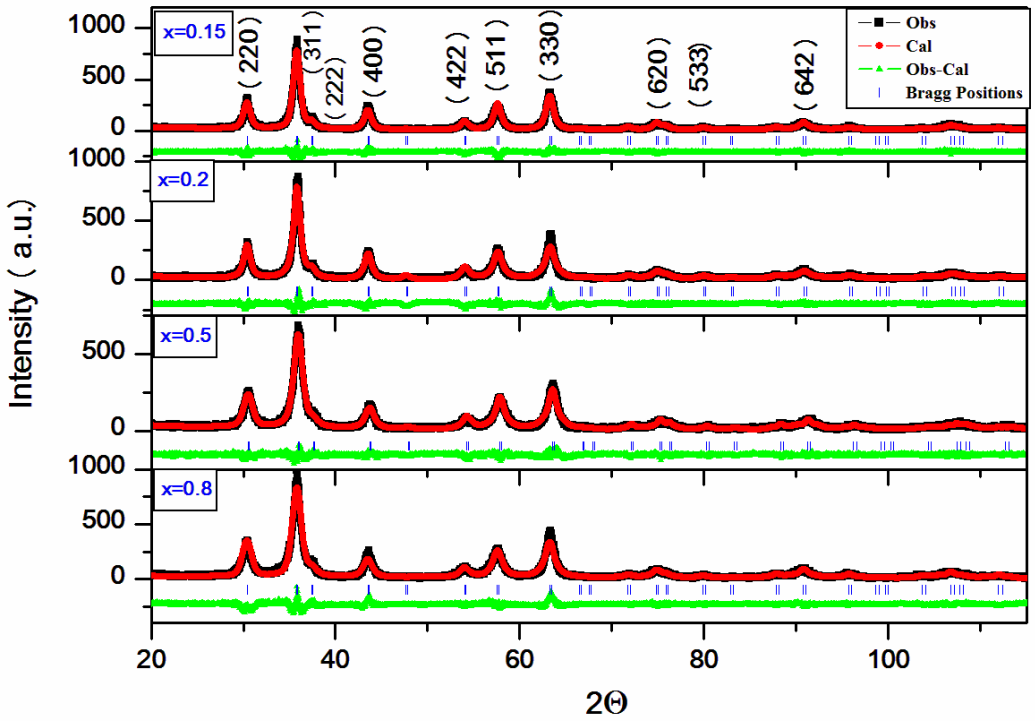

Fig. 7.2.1 X-ray diffraction (XRD) patterns of $Zn_xCo_{1-x}Cr_2O_4$ for x=0.15, 0.2, 0.5 and 0.8 fitted with the space group $Fd\bar{3}m$ using the Le-Bail profile refinement.

All peaks belong to pure cobalt chromite and no impurity peaks are observed. The Fulprof software was used to fit the XRD patterns with $Fd\bar{3}m$ space group. Fig. 7.2.1 depicts the observed, calculated and the difference plot. The Bragg peaks are represented by the tick marks above the difference plot. The lattice parameter (a) is obtained from Le-Bail profile refinement which decreases from 8.31 Å to 8.25 Å with increase in x from x=0.15 to 0.8. Even though the radius of Zn^{2+} is (0.74 Å) slightly higher than Co^{2+} ion (0.72 Å), we have observed a small reduction in unit cell volume with increase in Zn concentration. Melot et al. observed similar decrease in unit cell volume in bulk $Co_xZn_{1-x}Cr_2O_4$ [Melot et al. (2009)]. It could be due to less ionic nature of Zn than Co, and/or due to decrease in A-B repulsion. Further, Debye-Scherrer formula is used to estimate the mean crystallite size of the samples.

The crystallite size, $D_{XRD}= \frac{0.89\,\lambda}{\beta \cos \theta}$ **----------(7.1)**

β is defined as full width at half-maximum (FWHM) of the peak, Θ is the Bragg angle. The average crystallite size is found to be of the order of 10 nm for all samples.

7.2.1.2. X-ray Photoelectron Spectroscopy

The valance states of transition metals in $Zn_xCo_{1-x}Cr_2O_4$ (x=0.15, 0.2, 0.5, 0.8) are investigated by X-ray Photoelectron Spectroscopy (XPS). Fig. 7.2.2 (a) and 7.2.2 (b) depicts the characteristic core-level spectra of Co 2p and Cr 2p of $Zn_xCo_{1-x}Cr_2O_4$ (x=0.15, 0.2, 0.5, 0.8) which are fitted with XPS peak 4.1 software.

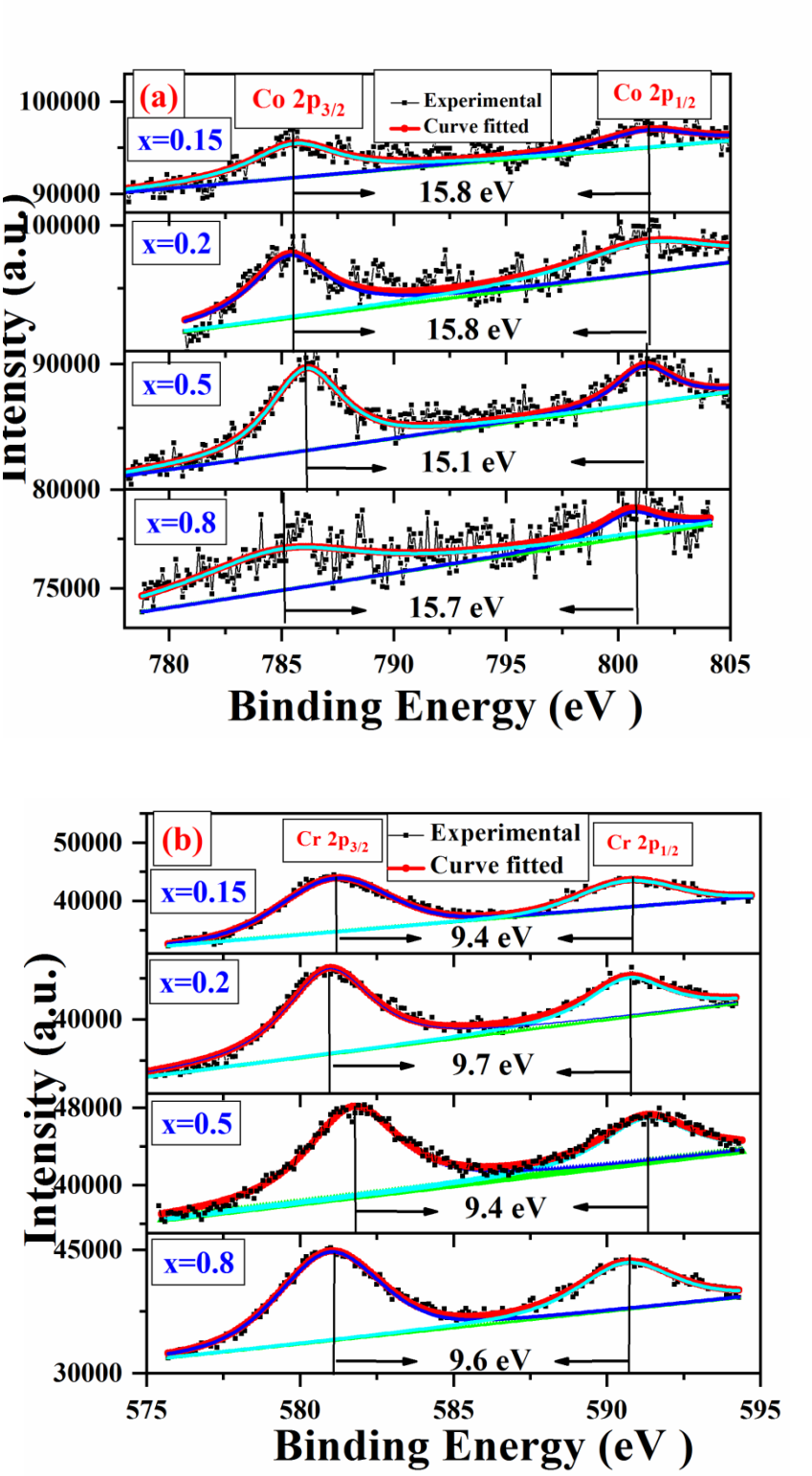

Fig. 7.2.2 (a) and (b) Fitted XPS spectra of Co and Cr for $Zn_xCo_{1-x}Cr_2O_4$ (x= 0.15, 0.2, 0.5 and 0.8).

Fig. 7.2.2 (a) shows two strong peaks at 785 and 801 eV which correspond to Co $2p_{3/2}$ and Co $2p_{1/2}$ respectively. The observed BE difference between $2p_{1/2}$ and $2p_{3/2}$ sublevels of Co 2p are found to be 15.8, 15.8, 15.1 and 15.7 eV for x=0.15, 0.2, 0.5 and 0.8 respectively. +2 oxidation state of Co is confirmed from the observed binding energy difference between two sublevels [Okamoto et al. (1975)]. Similarly, the two main peaks are observed around 981 and 591 eV, shown in Fig. 7.2.2 (b) corresponds to Cr $2p_{3/2}$ and Co $2p_{1/2}$ respectively. The obtained binding energy difference between $2p_{1/2}$ and $2p_{3/2}$ sublevels of chromium are 9.4, 9.7, 9.4 and 9.6 eV for x=0.15, 0.2, 0.5 and 0.8 respectively. The observed BE difference between sub levels of $2p_{1/2}$ and $2p_{3/2}$ of chromium confirms the +3 oxidation state [Okamoto et al. (1975)].

7.2.1.3. Extended X-ray Absorption Fine Structure

The cation distribution of $Zn_xCo_{1-x}Cr_2O_4$ (x= 0.15, 0.2, 0.5 and 0.8) is studied using Extended X-ray Absorption Fine Structure (EXAFS). The Co, Zn and Cr K-edges of EXAFS data have been analyzed using Athena and Artemis program coupled with the FEFF 8.0 code. The normalized absorption versus energy for Co K-edge is shown in Fig.7.2.3. By comparing the K-edge peak of Co, Cr and Zn with standard samples of CoO, YCr_2O_3 and ZnO, further we oserve that the valence states of Zn, Co and Cr are +2, +2 and +3 respectively.

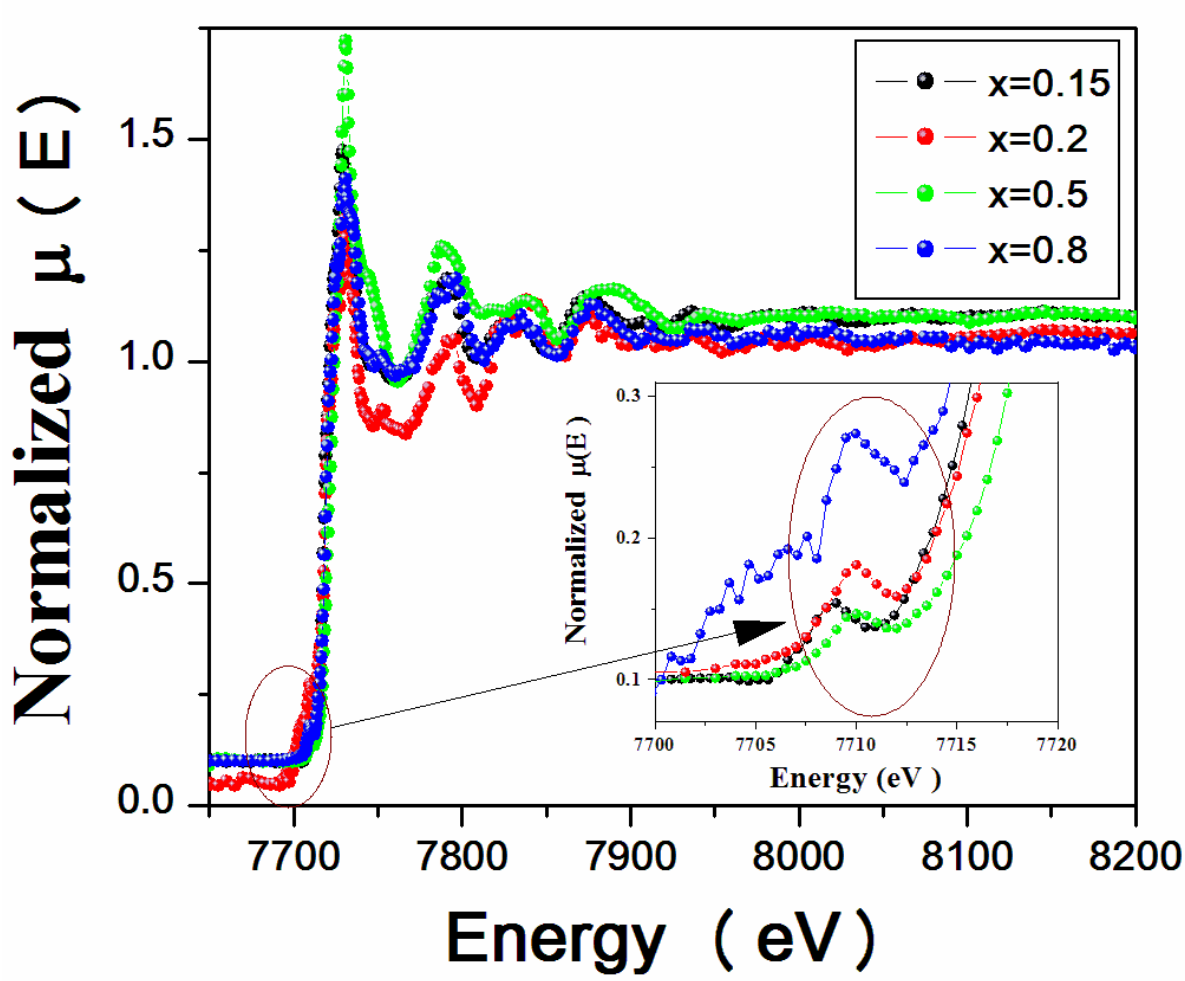

Fig. 7.2.3 EXAFS spectra of Co K-edge for $Zn_xCo_{1-x}Cr_2O_4$ (x=0.15, 0.2, 0.5, 0.8) nanoparticles. The expanded view of the pre-edge peak is shown in inset.

One can notice that the K-edge peak observed at 7710 eV does not change with x from 0.15 to 0.8. The main peak of Co K-edge shows a small pre-edge peak (Inset of Fig. 7.2.3) and is found to be in both Cr and Zn K-edges. While, the main peak of Co K-edge is ascribed to 1s to 4p transition, the pre-edge peak represent 1s to 3d quadrapole and from 1s to 3d/4p (hybridized orbitals) dipole transitions [Groot et al. (2001); Grunes et al. (1983)]. The degree of hybridization of transition metal 3d states with 4p states affects the pre-edge peak intensity in additive with low intensity of the quadrupole transition. This

inturn is affected by the degree of centrosymmetry of the photon absorber. Due to inversion symmetry, the mixing of the 4p and 3d orbitals is forbidden in octahedral site which is allowed in the tetrahedral symmetry [Groot et al. (2001); Grunes et al. (1983)]. Hence, the presence of pre-edge peak confirms that Co ions occupy the tetrahedral site. The absence of pre-edge peak in Cr K-edge confirms that Cr prefers to occupy the octahedral site. The increase in intensity of pre-edge peak Co with increase in Zn concentration indicates that Co prefers tetrahedral site. Further, the Fourier transform of the respective K-edge spectra gives the qualitative information about the local structure around Co, Zn, and Cr atoms.

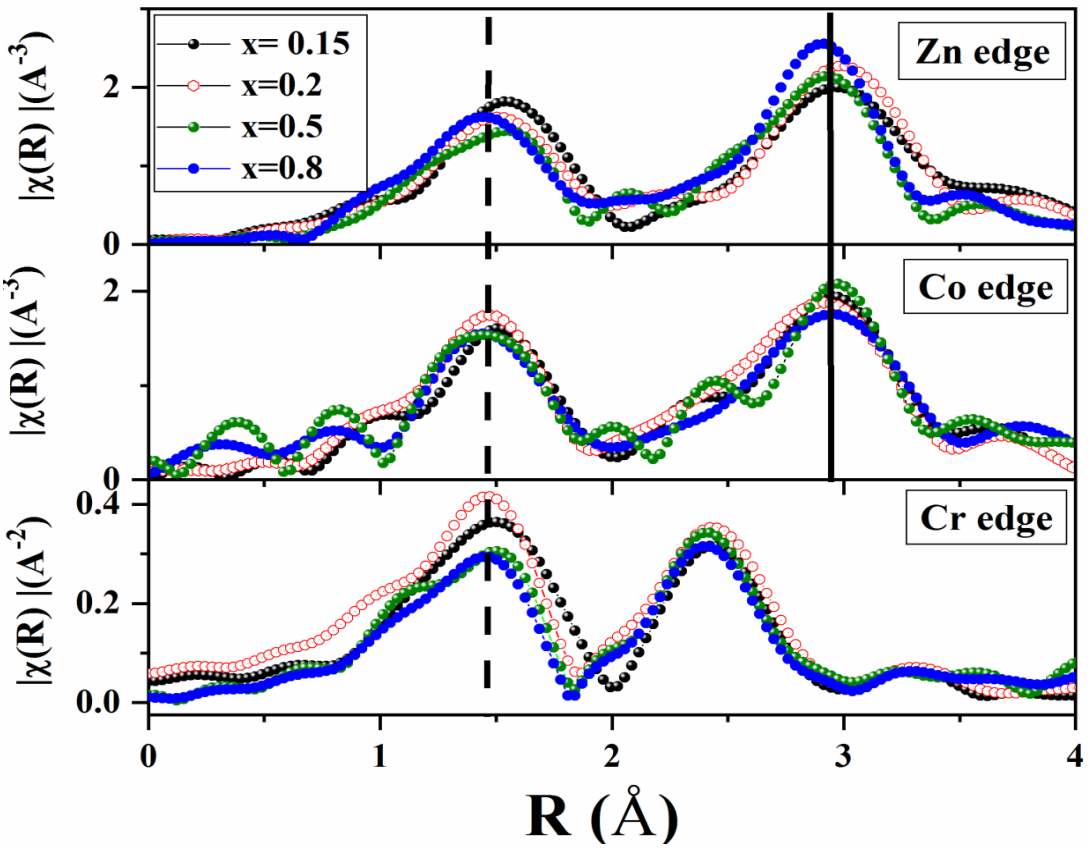

Fig. 7.2.4 Fourier transforms of χ(R) EXAFS for Zn, Co and Cr K-edges data.

The Fourier transform in R-space for Zn, Co and Cr are depicted in Fig. 7.2.4. In general, in ferrites, the cation distribution is obtained from the radial distance of the first coordination shell which observed at different radial distances. But in case of $CoCr_2O_4$, which is a normal spinel with Co preferring A site and Cr occupying B site, the radial distribution of the first coordination shell in Co and Cr environments is found to be same at 1.6 Å [Jagadish et al. (2016)]. The cation distribution is obtained by considering the position of second shell peak which is observed at different radial distances in Co and Cr environments. Similarly, in present case, Zn, Co and Cr K-edges, the first coordination shell is at ~1.6 Å. Hence, the cation distribution is obtained from the position of the second coordination shell. In the case of Zn and Co, the position of second peak is observed at r ~ 3 Å which indicates that Zn and Co prefer to occupy the A site. In case of Cr, the position of second peak is observed at r ~ 2.45 Å which indicates that Cr prefers to occupy the B site. With this information, we further fitted the reduced EXAFS data in R-space using Fourier transform in order to isolate the contribution of the short scattering paths. IFEFFIT (ARTEMIS) software is used to fit the background data, raw Fourier transform EXAFS spectra and energy calibrated spectra in Zn, Co and Cr edges for x=0.15, 0.2, 0.5 and 0.8. The bond distance (r) and mean-square disorder parameter (σ^2) are obtained from the fitting. The amplitude function (σ^2) is defined as the mean-square displacement of the path-length due to the thermal or static disorder and is strongly correlated with the number of nearest neighbors. The FEFF input file is generated with inputs of lattice parameters and atomic coordinates. It is also considered that Cr, Zn and/or Co as the core for the corresponding Cr, Zn and/or Co K-edge spectra. We have used the atomic coordinates of Co to fit the Zn K-edge as Zn replaces Co at A-site. The

experimental data is fitted up to 4 Å in the R-space and the results are shown in Fig. 7.2.5.

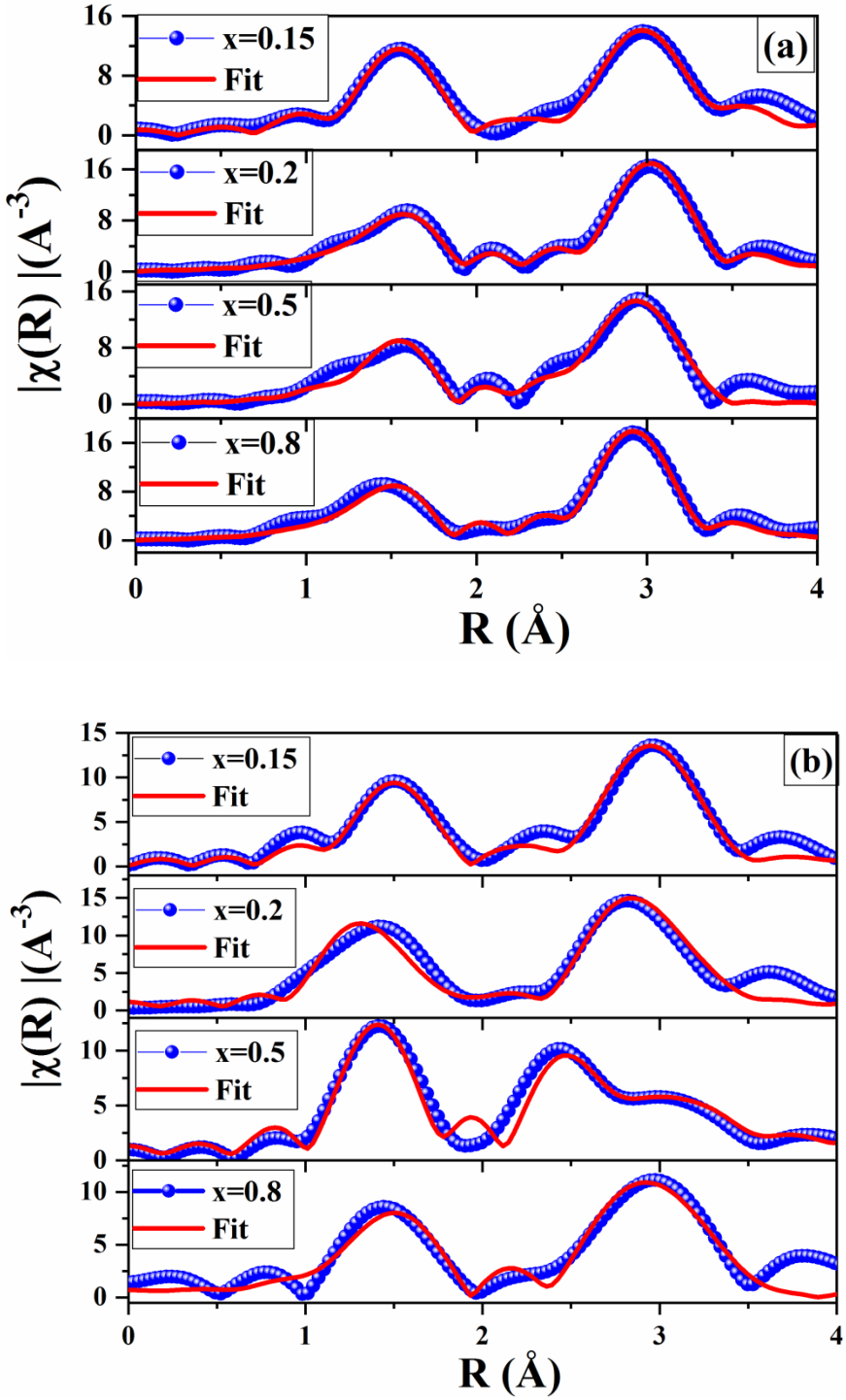

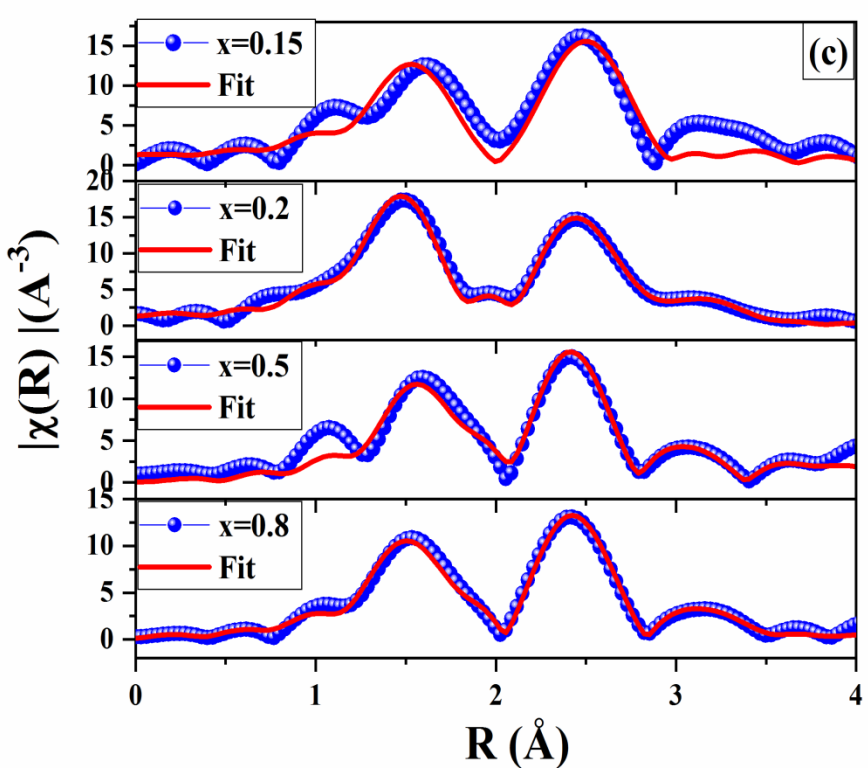

Fig. 7.2.5 (a) Real (r) parts of the phase plotted with fitted curves for $Zn_xCo_{1-x}Cr_2O_4$ (x=0.15, 0.2,0.5, 0.8) for **(a)** Zn K- edge, **(b)** Co K-edge and **(c)** Cr K-edge Fourier transform of EXAFS.

Table 7.2.1: Bond length, disorder factors deduced from EXAFS fitting of $Zn_xCo_{1-x}Cr_2O_4$ (x=0.15, 0.2, 0.5, 0.8) for (a) Zn K-edge (b) Co K-edge and (c) Cr K-edge respectively.

(a) Zn edge					
Path	**Parameter**	**x= 0.15**	**x= 0.2**	**x=0.5**	**x=0.8**
Zn-O	**r/^{o}A**	1.98	1.958	1.95	1.91
	σ^2	0.002	0.008	0.005	0.007
Zn-Cr	**r/^{o}A**	3.46	3.45	3.419	3.42
	σ^2	0.0055	0.006	0.0082	0.005
Zn-O	**r/^{o}A**	3.86	3.395	3.267	3.45
	σ^2	0.006	0.07	0.098	0.07
Zn-Zn	**r/^{o}A**	3.67	3.595	3.297	3.57
	σ^2	0.004	0.006	0.0063	0.005
(b) Co edge					
Path	**Parameter**	**x= 0.15**	**x= 0.2**	**x=0.5**	**x=0.8**
Co-Cr	**r/^{o}A**	1.95	1.81	1.86	1.94
	σ^2	0.0036	0.003	0.002	0.006
Co-Cr	**r/^{o}A**	3.42	3.34	3.32	3.42
	σ^2	0.004	0.00	0.009	0.005
Co-O	**r/^{o}A**	3.40	3.23	3.32	3.45
	σ^2	0.03	0.03	0.005	0.047
Co-Co	**r/^{o}A**	2.63	2.07	3.17	3.58
	σ^2	0.002	0.0	0.002	0.003
(C) Cr edge					
Path	**Parameter**	**x=0.15**	**x=0.2**	**x=0.5**	**x=0.8**
Co-O	**r/^{o}A**	1.956	1.927	1.96	1.978
	σ^2	0.005	0.004	0.007	0.0016
Cr-Cr	**r/^{o}A**	2.901	2.892	2.92	2.9204
	σ^2	0.004	0.009	0.0015	0.0031
Cr-Co	**r/^{o}A**	3.25	3.33	3.42	3.424
	σ^2	0.036	0.015	0.002	0.009

From Table 7.2.1, one can notice that the bond length (r) between the central atom and second coordination shell of Co, Zn and Cr are of the order of 3.42 Å, 3.46 Å and 2.91 Å. It is also observed that there is no significant change in bond length with increase in Zn concentration from x=0.15 to 0.8. Hence we conclude that Co and Zn ions occupy the A

site and Cr strongly prefers the B site. The results corroborates with our previous report on $CoCr_2O_4$ where we have shown that Co atoms are tetrahedrally coordinated by 12 Cr ions at 3.45 Å as second nearest neighbors and Cr atoms are octahedrally coordinated by 6 Cr ions at 2.96 Å as the second nearest neighbors [Jagadish et al. (2016)].

7.2.2. Magnetic Properties

7.2.2.1. Temperature dependent magnetization

The magnetic properties in $Zn_xCo_{1-x}Cr_2O_4$ (x=0.15, 0.2, 0.5, 0.8) nanoparticles are further studied using temperature dependent magnetization. The temperature dependent magnetization in zero-field-cooled (ZFC) and field-cooled (FC) condition at 500 Oe over a temperature range of 2-300 K is shown in Fig. 7.3.1.

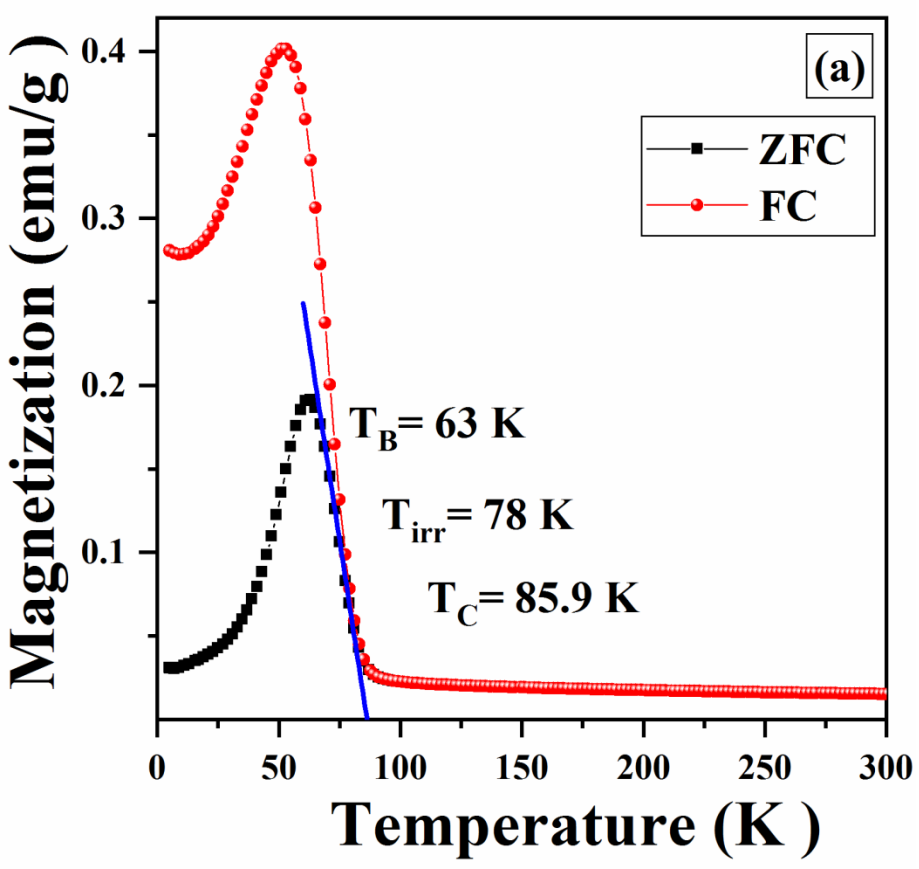

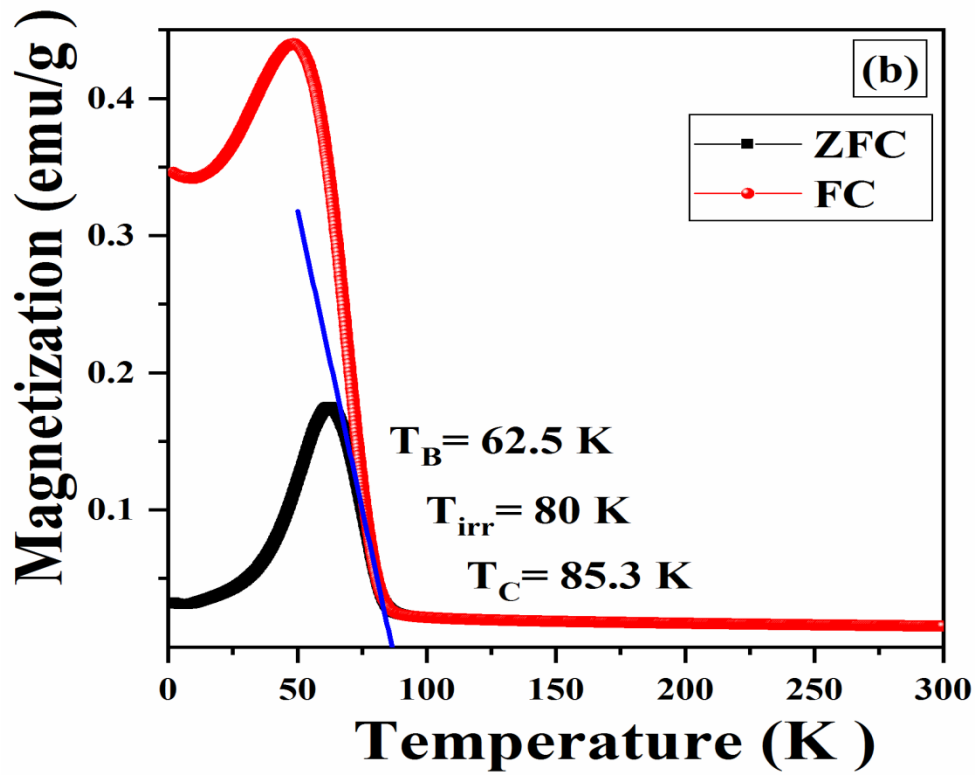
(b)
ZFC
FC
T_B= 62.5 K
T_{irr}= 80 K
T_C= 85.3 K
Magnetization (emu/g)
Temperature (K)
0.1
0.2
0.3
0.4
0
50
100
150
200
250
300

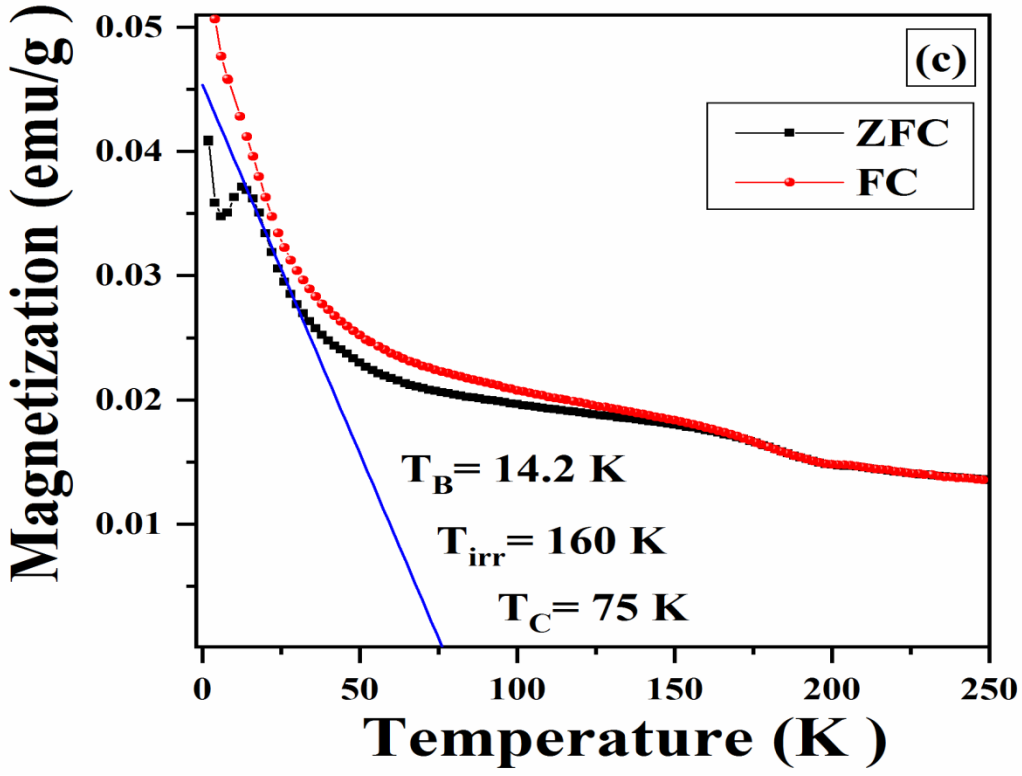
(c)
ZFC
FC
T_B= 14.2 K
T_{irr}= 160 K
T_C= 75 K
Magnetization (emu/g)
Temperature (K)
0.01
0.02
0.03
0.04
0.05
0
50
100
150
200
250

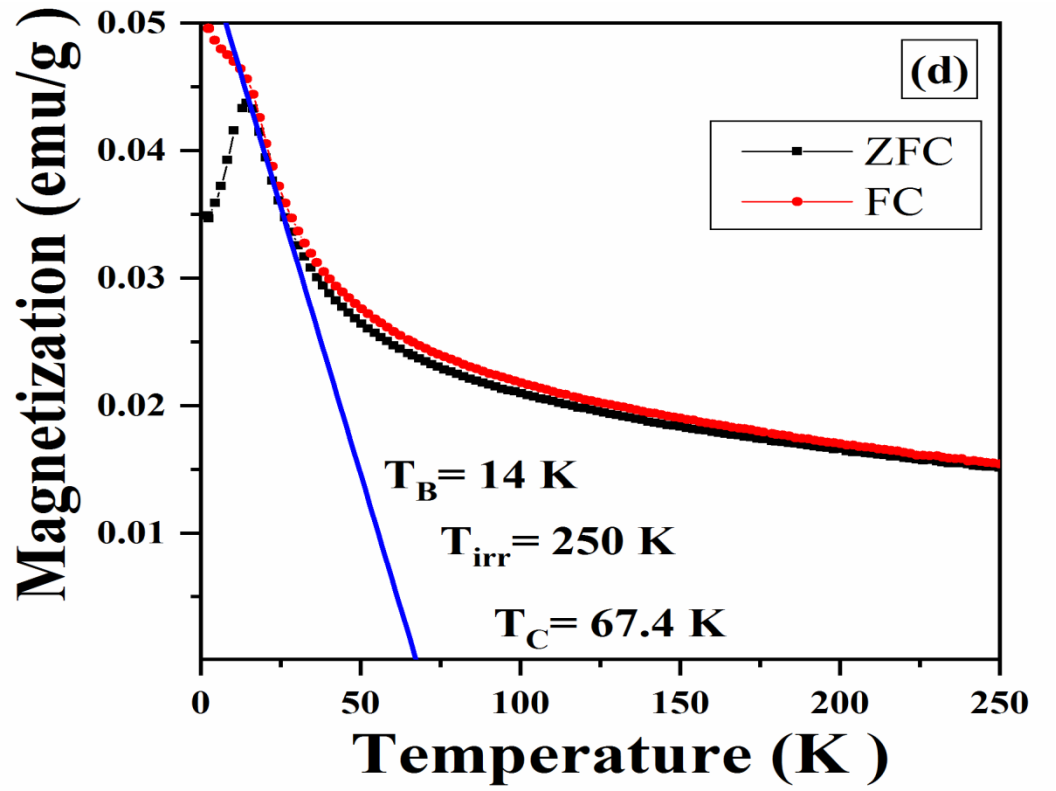

Fig. 7.3.1 Temperature dependent magnetization at 500 Oe for $Zn_xCo_{1-x}Cr_2O_4$ **(a)** x=0.15 **(b)** x=0.2 **(c)** x=0.5 and **(d)** x=0.8.

By cooling the sample from 300 K, the magnetization shows sudden change at a temperature at which paramagnetic to ferrimagnetic transition (T_C) is observed. While the rapid raise in magnetization is observed in x=0.15, 0.2, a linear change in magnetization is observed in x=0.5, 0.8 samples. The Curie temperature (T_C) is obtained from extrapolation of linear part of magnetization to zero in the high temperature regime which is found to be 85.9 K, 85.3 K, 75 K and 67.4 K for x=0.15, 0.2, 0.5 and 0.8 respectively. In general, T_C strongly depends on the A-B exchange interaction; the decrease in T_C with increase in Zn could be due to decrease in A-B exchange interaction. More non-magnetic Zn^{2+} ions replace the Co^{2+} ions with increase in Zn concentration. Hence, the A-B interaction reduces. The obtained value of T_C is higher than T_C of bulk $Zn_xCo_{1-x}Cr_2O_4$

reported by Melot et al. [Melot et al. (2009)]. They have observed T_C of 55 K at x=0.2 which is reduced to 8 K at x=0.8 in bulk $Zn_xCo_{1-x}Cr_2O_4$. By reducing the size, we have shown T_C of 85 K at x=0.2 reduced to 67.4 K at x=0.8. One fold increase in T_C at x=0.8 is surprising and could be attributed to finite size effect. Similarly in Mn-Zn ferrite nanoparticles, spinel ferrites, an increase in T_C has been reported by reducing the size to nanometer [Rath et al. (1999); Rath et al. (2002); Tang et al. (1991)]. One can also observe that, the value of T_C at x=0.15 is lower than T_C of x=0.05 and x=0.1, i.e. 90 K and 87.4 K [Fig. 6.2.2.1]. With decrease in temperature, FC and ZFC bifurcates at irreversible temperature, T_{irr} which are noted as 78, 80, 160 and 250 K for x=0.15, 0.2, 0.5 and 0.8 respectively. Further decrease in temperature both M_{ZFC} and M_{FC} increases and reaches to a maximum temperature (T_B). In a non-interacting particle system, the maximum temperature in a zero-field-cooled magnetization curve is the average blocking temperature of all the particles. The value of T_B is 63, 62.5, 14.2 and 14 K for x=0.15, 0.2, 0.5 and 0.8 respectively. Further decreasing the temperature below T_B, the magnetization of ZFC for x=0.5 increases with decrease in temperature. The magnetization at 2 K is 0.04 emu/g, which is slightly higher than magnetization at T_B. The increase in the magnetization at temperature below T_B is attributed to the relaxation of the particles which have equal or slightly higher blocking temperature. The decrease in blocking temperature 63 K to 14 K with increase in x from 0.15 to 0.8 is due to decrease in strength of superexchange interaction between A and B sites [shahane et al. (2010)]. While T_C and T_B decrease, T_{irr} increases with increase in x.

Table 7.2.2 Curie temperature (T_C), irreversible temperature (T_{irr}), blocking temperature (T_B) and reported curie temperatures in bulk samples.

X	**T_C (K)**	**T_{irr} (K)**	**T_B (K)**	**Reported T_C in bulk (K)** [Melot et al.(2009)]
0.15	85.9	78	63	-
0.2	85.3	80	62.5	55
0.5	75	160	14.2	-
0.8	67.4	250	14	8

From Table 7.2.2, one can also observe that the T_{irr} is greater than T_B for all samples. While There is no evidence of spin-spiral transition (T_S) and lock-in transitions (T_L) as are present in x= 0.05 and 0.1 [discussed in chapter 6].

7.2.2.2. Field dependent magnetization

Further, the field dependent magnetization measurement is performed in order to find the relative alignments of spins and their magnitude. The magnetization is measured after cooling the sample under zero field cool (ZFC) condition and by applying magnetic field of 140 kOe at 2 K and 20 K. The variation in magnetization (M) with magnetic field (H) at 2 K and 20 K is shown in Fig. 7.3.2.

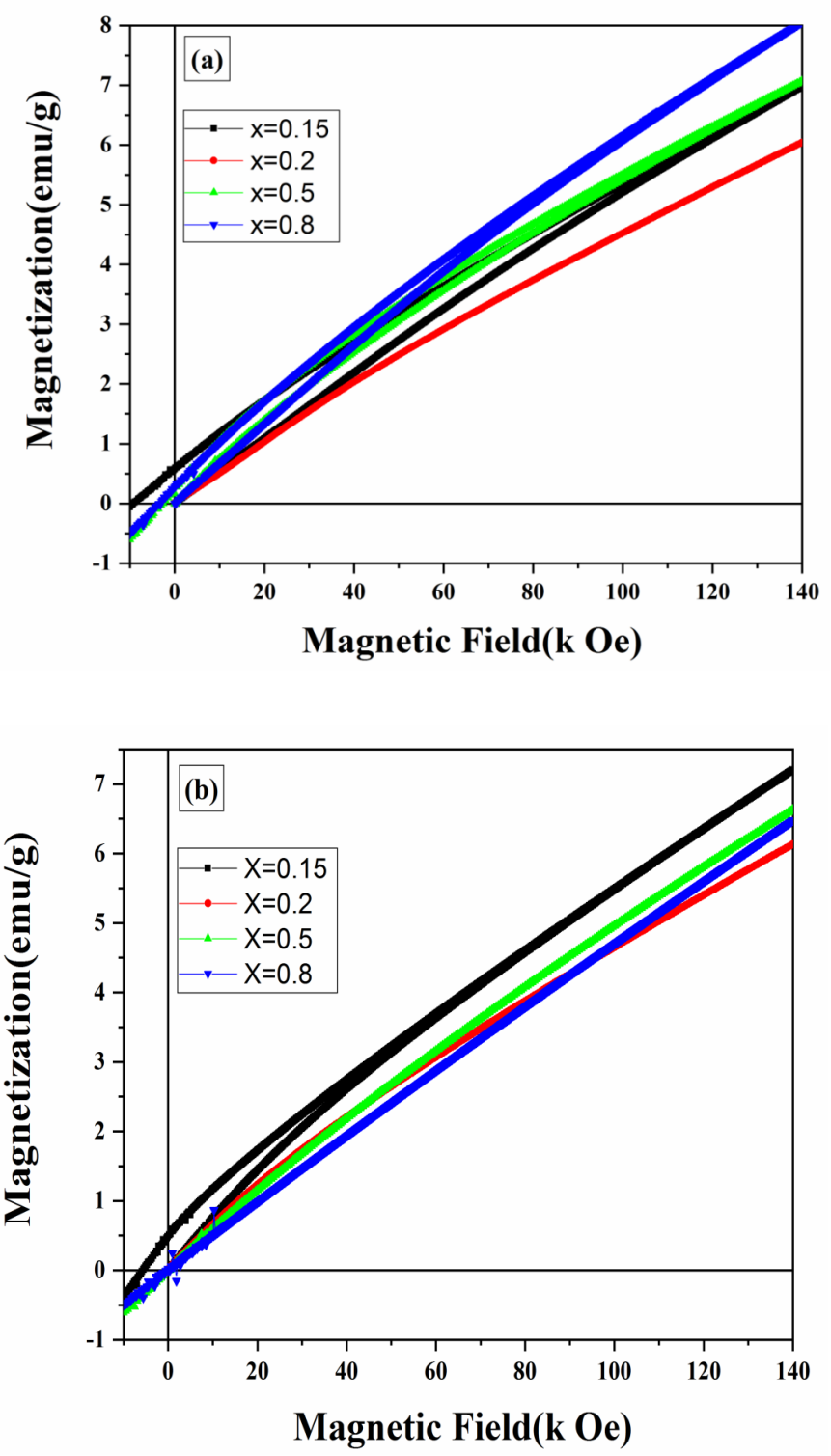

Fig. 7.3.2 Magnetic field (H) dependent magnetization at (a) 2 K and (b) 20 K for $Zn_xCo_{1-x}Cr_2O_4$ (x=0.15, 0.2, 0.5, 0.8).

The magnetization doesn't saturate upto 140 kOe irrespective of measuring temperatures i.e., at 2 K and 20 K. The non-saturation of magnetization results from the large contribution of disordered spins at the surface. Such behavior is also reported in several ferrimagnetic systems [Maaz et al. (2009)]. The maximum magnetization (M_{max}) is noted as 0.28, 0.24, 0.29 and 0.33 μ_B/f.u. for x=0.15, 0.2, 0.5 and 0.8 respectively. We have also observed that M_{max} decreases from 0.36 to 0.32 μ_B/f.u. with increase in x from 0.05 to 0.1 [Fig. 6.2.2.6 of chapter 6]. From Fig. 7.3.3, the experimental magnetization decreases from 0.366 to 0.248 μ_B/f.u. with increase in x from 0.05 to 0.2 and then increases to 0.334 μ_B/f.u. for x=0.8. The theoretical moments are calculated (M_B-M_A) as 3.15, 3.3, 3.45, 3.6, 4.5 and 5.4 μ_B/f.u. for x=0.05, 0.1, 0.15, 0.2, 0.5 and 0.8 respectively. The experimental and calculated moments compared and are shown in Fig. 7.3.3. The experimental magnetic moments are found to be one order magnitude less than the calculated moments. The reduction in magnetization could be due to the existence of random canting of spins at the surfaces due to nanometer size of the particles [Coey et al. (1971)]. While the calculated moment increases linearly, the experimental moment decreases up to x=0.2 and then increases for x=0.5 and 0.8 as shown in Table 7.2.3.

Table 7.2.3 Maximum magnetization, coercive field and theoretical moment for 0.05≤x≤0.8

X	M_{max} (μ_B/f.u)	H_C (k Oe)	M_{theory}
0.05	0.3661	3.2	3.15
0.1	0.3247	5.2	3.3
0.15	0.2844	9	3.45
0.2	0.2488	5.3	3.6
0.5	0.2909	2.6	4.5
0.8	0.3345	3.2	5.4

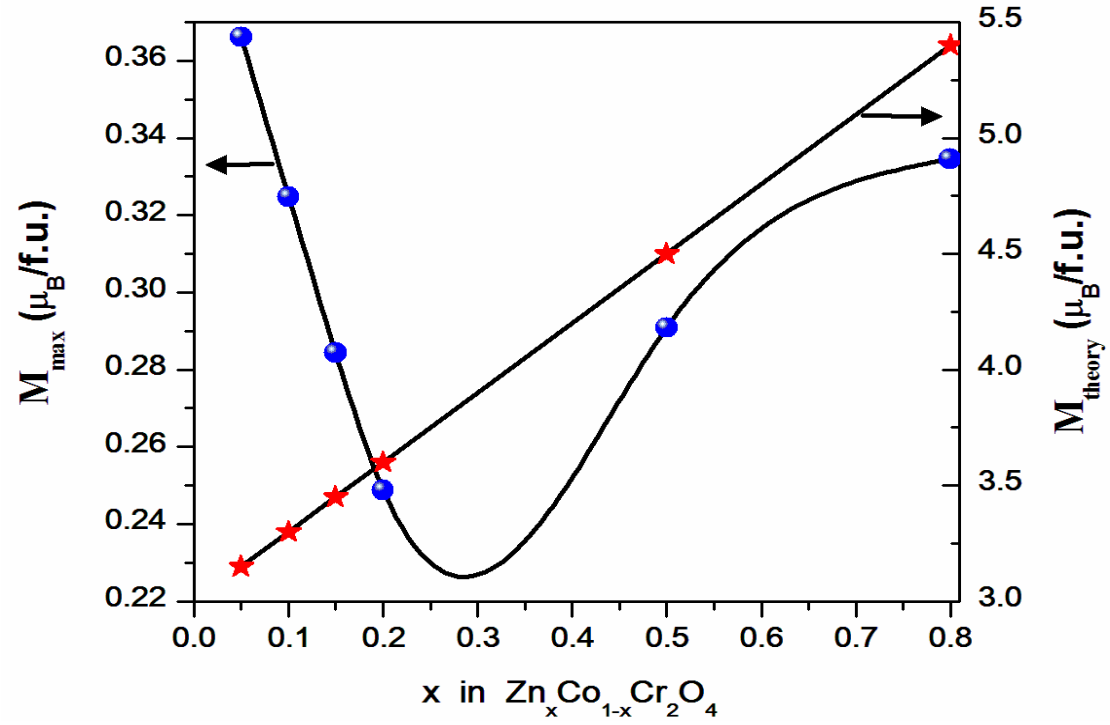

Fig. 7.3.3 Experimental and calculated magnetization varying with x in $Zn_xCo_{1-x}Cr_2O_4$ (x =0-0.8).

In general, mixed ferrites containing zinc, like Ni-Zn, Co-Zn and Mn-Zn ferrites show an increase in net magnetic moment after addition of 10% of Zn [Cullity (1978)]. This could be explained as the net moment in A site decreases because of non-magnetic Zn ions in A site. While the Fe ions in B site have parallel moments because of strong A-B interaction, the net moment increases in contrast with the calculated moments. Continued with further addition of Zn, the net moment decreases as A site moments became weak to affect the B site moments. In contrast to the above result, the net moment decreases in $CoCr_2O_4$ upto 20 mol% of Zn and then increases up to 80 mol%. This could be explained by considering competing exchange forces between the strong BB interaction and the weak AB interaction as non-magnetic Zn^{2+} ions replace Co^{2+} in A site. One can notice that, with increase in Zn concentration from 0.15 to 0.8, the coercivity decreases from 9 kOe to 3.2 kOe. The coercivity at 2 K is found to be two orders magnitude higher than bulk $CoCr_2O_4$. However, 10 nm $CoCr_2O_4$ particles show the coercivity of 7.6 kOe at 2 K [Fig. 4.2.9 (a) of Chapter 4] and decreases to 3.2 kOe with addition of 5 mol% of Zn [Fig. 6.2.2.6 of Chapter 6]. It is reported that addition of Zn in $CoFe_2O_4$ results in decrease in saturation magnetization and coercivity [Franco et al. (2013)]. The decreasing trend is an indication of Co^{2+} is being replaced by Zn^{2+} ions in $Co_{1-x}Zn_xFe_2O_4$. Similarly in the present case, after incorporation of Zn ions in $CoCr_2O_4$, the coercivity decreases as Zn^{2+} ions replace Co^{2+} ions in A site.

7.2.2.3. Temperature dependent ac susceptibility

The magnetic ordered state of nanoparticles is examined through the ac susceptibility measurements ($\chi'$and χ'') with varying temperature and frequency. he real (χ') part of ac

susceptibility at 3, 31, 229 and 966 Hz, with varying temperature from 2-300 K, for x= 0.15, 0.2, 0.5 and 0.8 are shown in Fig. 7.3.4.

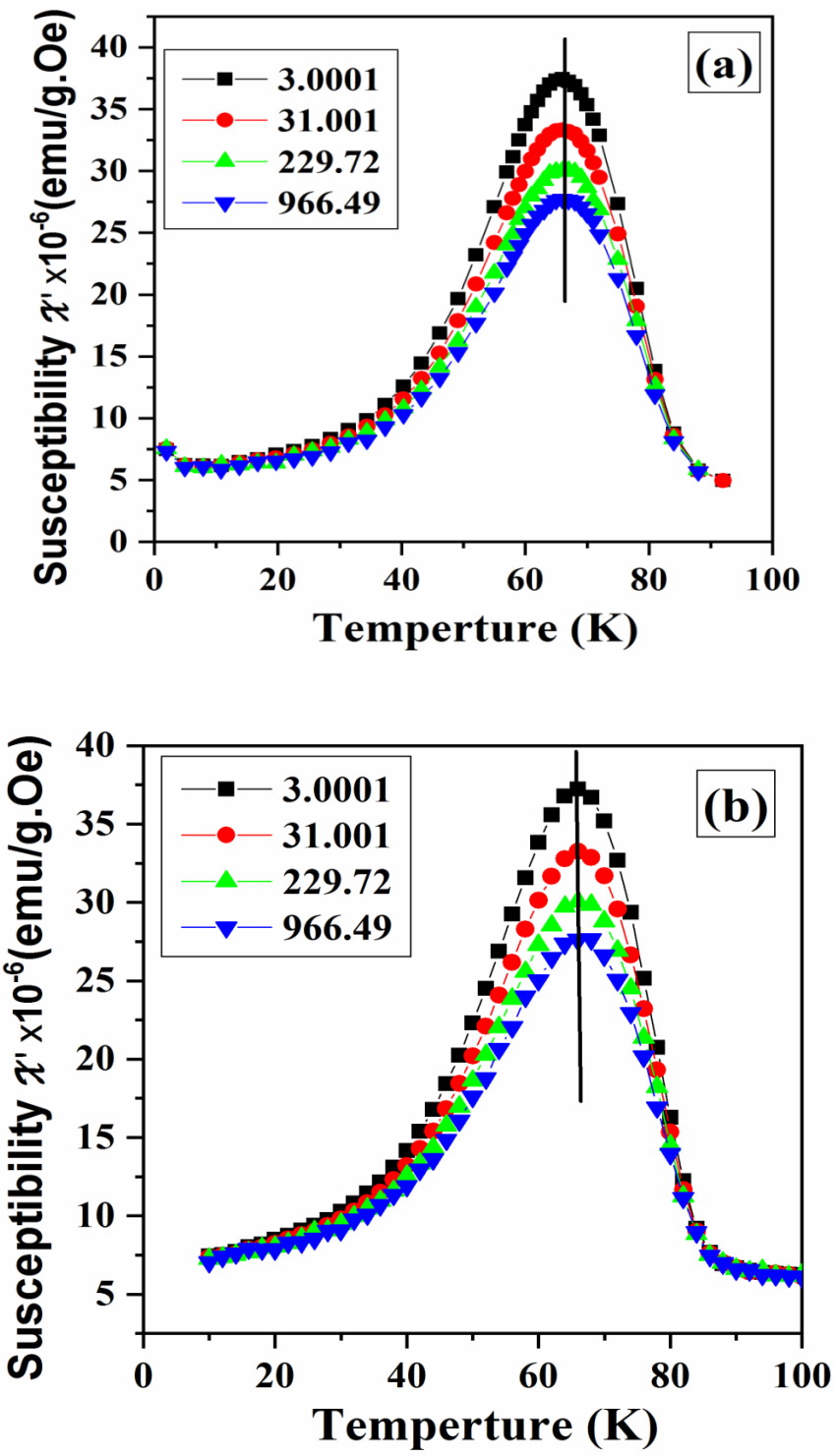

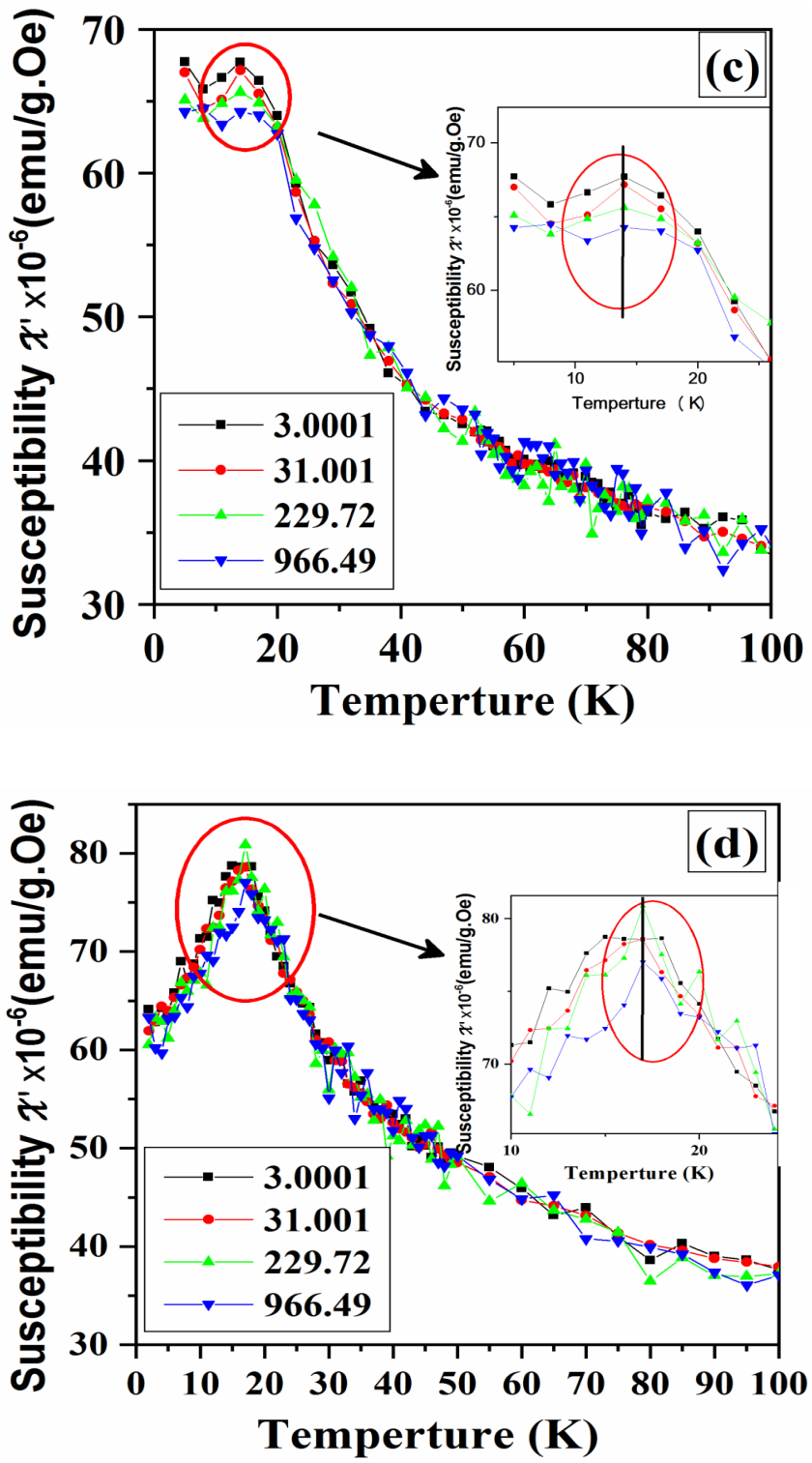

Fig. 7.3.4 Real part of ac susceptibility versus temperature at different frequencies 3, 31, 230 and 966 Hz for $Zn_xCo_{1-x}Cr_2O_4$ (a) x=0.15, (b) x=0.2, (c) x=0.5 and (d) x=0.8.

From the real part of ac susceptibility, there is shift in the peak with temperature and varying frequency in all samples. In both spin glass and superparamagnetic systems, such frequency dispersion of ac susceptibility is common. However, in present case, there is no shift in T_B with frequency which eliminates the possibility of non-interacting superparamagnetic and spin-glass nature of the particles.

7.3. Conclusions

In this chapter, we have studied the structure, cation distribution and magnetic properties of $Zn_xCo_{1-x}Cr_2O_4$ (x=0.15, 0.2, 0.5, 0.8) nanoparticles which were synthesized through conventional co-precipitation technique. XRD patterns confirmed the cubic spinel structure without having any impurity. Lattice parameter decreased with increase in Zn concentration, due to less ionic nature of Zn than Co, and/or due to decrease in A-B repulsion. The cation distribution of $Zn_xCo_{1-x}Cr_2O_4$ studied through EXAFS confirmed that while Cr^{3+} ions preferred B site, Zn^{2+} and Co^{2+} ions occupied the A site. No change in cation distribution by reducing the particle size was observed from EXAFS. From dc magnetization, with increase in x from 0.15 to 0.8, we revealed that the Curie temperature (T_C) decreased from 85.9 K to 67.4 K. The observed value of T_C was higher than T_C of bulk $Zn_xCo_{1-x}Cr_2O_4$. The increase in T_C by one fold at x=0.8 by reducing the particle size was ascribed to finite size effect. In contrast to the Zn based ferrites, the net moment decreased in $CoCr_2O_4$ with addition of 20 mol% of Zn and then increased up to 80 mol%. Due to the existence of random canting of spins at the surfaces in particles of nanometer size, the experimental magnetic moments were found to be one order magnitude less than the calculated values. Temperature dependent ac magnetic susceptibility measurement

showed no dispersion behavior with frequency which confirmed the absence of superparamagentic and spin-glass behavior in these particles.